PCCP

RSC Publishing

PAPER

View Article Online
View Journal | View Issue

Cite this: *Phys. Chem. Chem. Phys.*, 2013, **15**, 3535

Hierarchical nanostructured core–shell Sn@C nanoparticles embedded in graphene nanosheets: spectroscopic view and their application in lithium ion batteries†

Dongniu Wang,[ab] Xifei Li,[a] Jinli Yang,[a] Jiajun Wang,[a] Dongsheng Geng,[a] Ruying Li,[a] Mei Cai,[c] Tsun-Kong Sham*[b] and Xueliang Sun*[a]

Received 22nd November 2012,
Accepted 8th January 2013

DOI: 10.1039/c3cp44172e

www.rsc.org/pccp

Hierarchical carbon encapsulated tin (Sn@C) embedded graphene nanosheet (GN) composites (Sn@C–GNs) have been successfully fabricated *via* a simple and scalable one-step chemical vapor deposition (CVD) procedure. The GN supported Sn@C core–shell structures consist of a crystalline tin core, which is thoroughly covered by a carbon shell and more interestingly, extra voids are present between the carbon shell and the tin core. Synchrotron spectroscopy confirms that the metallic tin core is free of oxidation and the existence of charge redistribution transfer from tin to the carbonaceous materials of the shell, facilitating their intimate contact by chemical bonding and resultant lattice variation. The hybrid electrodes of this material exhibit a highly stable and reversible capacity together with an excellent rate capability, which benefits from the improved electrochemical properties of tin provided by the protective carbon matrix, voids and the flexible GN matrices.

Introduction

With increasing demand for lithium ion batteries both in scientific and industrial fields, greater efforts have been devoted recently to fabricating functional nanocomposites, enabling the synergic effect of the individual unique properties of different components in the composite.[1,2] In general, constructing such a novel architecture can lead to higher energy density and cyclic durability.[3–5] Tin based materials have attracted considerable attention as anode candidates owing to their high theoretical capacity (about 994 mA h g^{-1}),[6] competitive cost, and easy processing. Nevertheless, there are critical problems hindering the practical implementation of this material, including the associated pulverization and capacity fading originating from a drastic volume change (over 250%) during the lithium insertion–extraction electrochemical process.[7,8]

Currently, two substantial avenues are applied collectively to circumvent these problems focusing on (i) tuning the morphologies of Sn into nanostructures and (ii) exploiting ideal matrices confining the volume change by the so-called "cushion effect".[3–5] As a result, many designs of Sn based nanocomposites are driven by the possibility of combining their high lithium storage properties with enhanced stability.[9–12] Nano-sized carbon additives, for example graphene, are considered as one of the most promising candidate materials in energy storage field due to their intriguing features such as large surface area (more than 2630 m^2 g^{-1}), high electronic conductivity, superior mechanical flexibility, and high theoretical capacity (786 mA h g^{-1}).[13–17] Because graphene can effectively buffer the volume change during cycling, applying graphene as a matrix to incorporate metal or metal oxide for nanoarchitectured composites could result in electrodes with superior durability. Various hybrids including Co_3O_4–graphene,[18] Fe_2O_3–graphene,[19] Sn–graphene,[20] SnO_2–graphene[21–23] *etc.* have been synthesized and enhanced electrochemistry performance compared with the bare metal or metal oxides has been demonstrated. Meanwhile, the design of core–shell nanostructures also achieved improved electrochemical performances, such as SnO_2@C[24,25] and Sn@C[26,27] nanostructured systems. Wang *et al.* have successfully synthesized nanocomposites based on core–shell Sn@C nanowires and SnSb@C nanoparticles hybridised with graphene.[26,27]

[a] *Department of Mechanical and Materials Engineering, University of Western Ontario, London, Ontario, N6A 5B9 Canada. E-mail: xsun@eng.uwo.ca; Tel: +1 519 661-2111 ext. 87759*

[b] *Department of Chemistry, University of Western Ontario, London, Ontario, N6A 5B7 Canada. E-mail: tsham@uwo.ca; Tel: +1 519 661-2111 ext. 86341*

[c] *General Motors R&D Center, Warren, 48090-9055, MI, USA*

† Electronic supplementary information (ESI) available: Experimental part, SEM image and TEM image of GNs, CV of Sn@C composites, Raman spectra, TGA curves of Sn@C and Sn@C–GN composites and TEM image of Sn@C–GN and Sn@C composites after 100 cycles. See DOI: 10.1039/c3cp44172e

The nanocomposites exhibited radically improved lithium storage capabilities and rate performance. However, the procedures are complicated involving multiple steps; in addition toxic reagents such as $NaBH_4$ and post heat treatment are required, which results in high cost and complicated parameters. More importantly, there is no fundamental study of the interaction between tin and carbon with regards to the electrochemical performance.

X-ray absorption near-edge structure (XANES) spectroscopy, which tracks the modulation of the X-ray absorption coefficient above an absorption edge of a core level of an element in a chemical environment, has been proved a powerful technique in unveiling the chemical structure and bonding between metal oxides and carbon nanotubes, such as SnO_2–CNTs,[28] RuO_2–CNTs[29] *etc.* Nevertheless, for hierarchical core–shell Sn@C nanocomposites, few work has been reported on the interaction between the Sn and carbonaceous materials by XANES, which is crucial for understanding the mechanism behind the improved electrochemical performances. Here, we present a facile and scalable one-step CVD method to synthesize Sn@C–GN composites. The hierarchical Sn@C core–shell nanostructures were anchored on GNs uniformly and densely with the crystalline Sn core and the carbon shell intact. XANES at relevant edges unveils the intimate correlation between metallic tin and surrounding carbonaceous materials, which immobilizes Sn into the carbon shell or GNs and compresses the lattice of Sn atoms. It is shown that the hybrid composite exhibits both highly reversible lithium storage properties and an excellent rate capability benefiting from the synergic effect of each component in the composite.

Results and discussion

The Sn@C–GN composites are synthesized by a fast, simple and scalable one-step CVD procedure. The following description is consistent with the observation reported in subsequent sections. First, ethylene reduces SnO_2 supported on GNs to metallic Sn nanoparticles, and then carbon, originating from the decomposition of ethylene, forms a shell at the surface of Sn nanoparticles (carbon has low solubility in tin during the CVD process). It should be noted that the Sn nanoparticles discussed here are in the liquid state at 800 °C and thus accompanying possible coalescence between separated nanoparticles could take place, leading to the increase in particle size. It is worth mentioning that the anchoring of tin oxide nanoparticles on GNs greatly avoids the merge. In another way, once the carbon shell is formed, it can serve as a geometrical separator and thus the aggregation of Sn nanoparticles can be effectively inhibited. In the subsequent cooling process, the Sn droplet transforms into solid Sn nanoparticles, accompanied with volume shrinkage, resulting in void space at the interface of the Sn core and the carbon shell. During the entire fabrication process, the GNs remain as a stable substrate for *in situ* nanocomposite formation. The growth process of Sn@C–GN hierarchical nanostructures is illustrated in Scheme 1.

Fig. 1 shows the X-ray diffraction (XRD) patterns of Sn@C, Sn@C–GN nanocomposites and GNs. Only one broad peak centered at 28.4° was detected in GNs, which is attributed to the (002) facet. For Sn@C and Sn@C–GN hybrids, all strong peaks match well with those of the β-Sn nanocrystals (PDF: 89-2761). It is noted that Sn@C–GN nanocomposites exhibit broader diffraction patterns compared with that of Sn@C composites, indicating a smaller tin particle size. Based on the (200) peak, the average crystal size of tin particles in Sn@C–GN nanostructures is around 75.6 nm according to Scherrer's equation. Moreover, there are no obvious peaks indexed for carbonaceous materials such as GNs or the carbon shell due to their low crystallinity. It should also be noted that no SnO_2 characteristic peaks were identified, indicating that the original SnO_2 was completely reduced to Sn by ethylene at 800 °C.

Fig. S1 (ESI†) shows the typical scanning electron microscopy (SEM) and transmission electron microscopy (TEM) images of GNs. It can be seen that GNs are composed of layered platelets with a curved structure. The ripped nanosheets exhibit high transparency for electrons under SEM and TEM, due to their ultrathin layers. The morphology of Sn@C nanocomposites is shown in Fig. 2a. Sn nanoparticles exhibit a non-uniform size distribution from 50 nm up to 2 μm combined with a carbon shell with a thickness of around 10 nm. In contrast, Fig. 2b confirmed that the morphologies of Sn@C–GNs are indeed GN supported core–shell structures. It can be seen that the Sn@C nanostructure is distributed densely on GNs with a more uniform size compared with Sn@C nanostructures without GNs. Interestingly, from low magnification SEM images (the inset of Fig. 2b), the layered morphologies could still be easily observed,

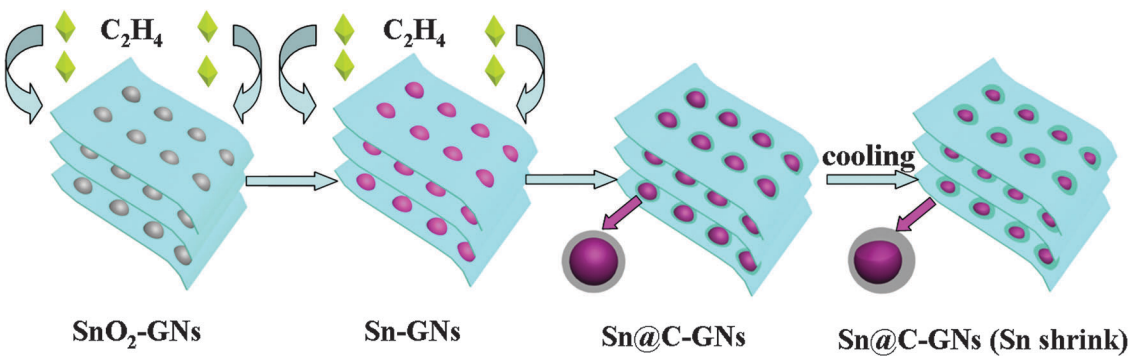

Scheme 1 Schematic sketch for the Sn@C–GN composite growth procedure.

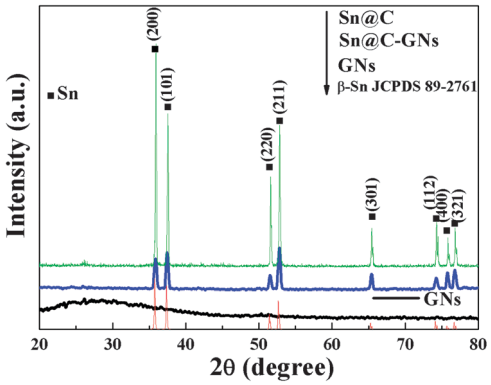

Fig. 1 XRD patterns of GNs, Sn@C and Sn@C–GN composites.

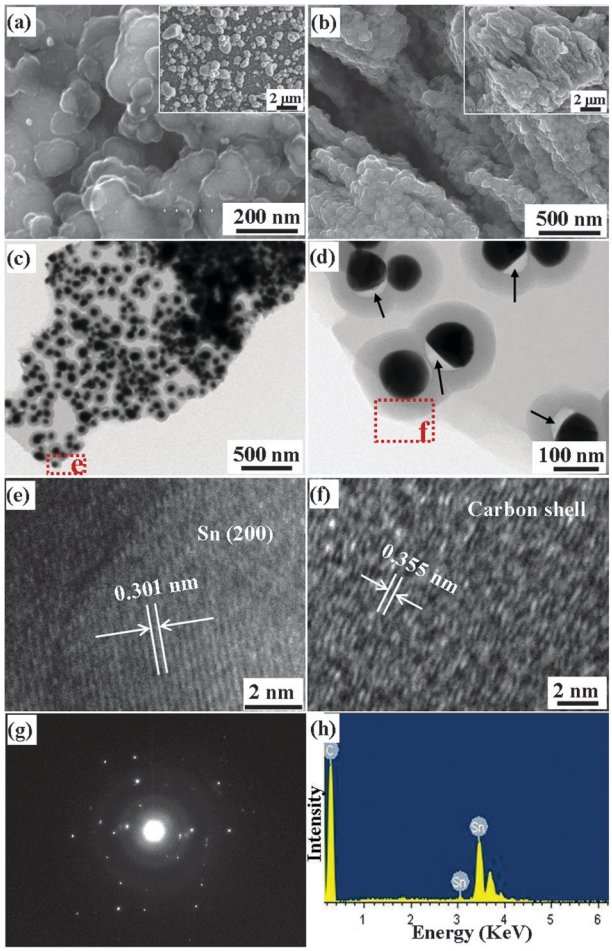

Fig. 2 SEM images of (a) Sn@C composites and (b) Sn@C–GN nanocomposites (insets show the relevant low magnification images); (c) and (d) TEM images and (e) and (f) HRTEM images of Sn@C–GN nanocomposites at red rectangular regions e (tin core) and f (carbon shell); (g) SAED patterns; (h) EDS patterns of Sn@C–GN nanocomposites.

indicating that GNs served as a stable support for deposition of Sn@C composites. Meanwhile, deposited Sn@C nanostructures effectively spatially inhibit the assembly of GNs. Fig. 2c and d show the TEM image of Sn@C–GN nanostructures. With GNs, the supported Sn@C nanostructure exhibits a uniform thickness of the outer carbon shell around 50 nm and a diameter of the inner Sn core between 60 nm and 100 nm. Compared with Sn@C without GNs, the significantly improved uniformity of Sn@C–GNs is due to the spatial separation of Sn nanoparticles and immobilization by GNs, preventing coalescence between Sn nanoparticles and the resultant irregular increase in particle size. Also, SnO_2 are widespread and well dispersed onto GNs, the two dimensional open system facilitates the diffusion of ethylene gas, introducing more sites for reaction between SnO_2 and ethylene due to a large surface to volume ratio, accelerating the reaction rate of ethylene with SnO_2. As a result, the formation rate of a carbon shell is faster, which could effectively prevent the liquid tin droplet from further agglomeration. The outside carbon shell could also help to buffer the volume change of Sn anodes during cycling, thus improving their cycle life.[9] For Sn@C without GNs, the partial agglomeration of Sn nanoparticles is inevitable due to the lack of separation and immobilization impacts provided by GNs, as illustrated in the inset of Fig. 2a, the size of some Sn particles increases up to 2 μm. Meanwhile, it has a thinner carbon shell (around 10 nm) compared with that of Sn@C–GNs synthesized under the same reaction conditions (*e.g.* time, temperature and flow rate of carrier gas), which could be attributed to a relatively slower deposition rate of carbon caused by limited reaction sites. Intriguingly, close observation of the Sn@C–GN systems reveals voids between the Sn core and the carbon shell, as indicated by black arrows in Fig. 2e. This is due to the contraction of Sn nanoparticles, that is, the liquid Sn obtained at high temperature (800 °C) would solidify with shrinkage of volume when the temperature is below the melting point of the Sn metal (231.93 °C) during the cooling process. Thus, the encapsulation of Sn by the carbon shell must have taken place at high temperature. It is noted that the voids produced here can offer extra space to relieve the stress and mitigate other adverse effects accompanied with expansion/contraction of Sn anodes during the lithium alloying and dealloying processes, combining the core–shell structure and the flexible graphene matrix, therefore improved electrochemical performances are expected.

To further clarify the structure and crystallinity of the Sn core and the carbon shell, high resolution TEM images taken from two areas highlighted with red rectangular regions as "e" and "f" in Fig. 2, are shown in Fig. 2e and f, respectively. Fig. 2e shows the lattice image of the exposed tin core from a broken Sn@C–GN nanostructure, the lattice fringe with a measured inter-planar distance of 0.301 nm matches well with the $\{200\}_{Sn}$ set of planes, indicating that the inner core is pure metallic Sn. Fig. 2f shows the lattice image of the carbon shell taken at the exterior shell of an intact Sn@C nanoparticle. It is found that the carbon layers are composed of staggered and shortened graphene sheets with a calculated lattice fringe of 0.355 nm, which is slightly larger than the standard graphitized carbon (0.335 nm). The swollen carbon layers could offer more room to facilitate lithium diffusion. The crystalline Sn and low crystallized carbon shell are further proved from the selected area electron diffraction (SAED) patterns from diffraction dots (tin) and weak rings (carbon), as shown in Fig. 2g. Energy dispersive

spectroscopy (EDS) patterns of Sn@C–GN nanocomposites (Fig. 2h) also illustrate that only Sn and C are detected in the composites, indicating that all SnO_2 have been totally reduced to Sn, which is in good agreement with the XRD results. Based on these desirable structures – the flexible GNs, the outside carbon shell, the well spatially separated Sn@C nanostructures and the voids between the Sn@C nanostructures – the hierarchical Sn@C–GN nanocomposites are anticipated to show excellent battery performances.

The Sn@C and Sn@C–GN nanostructures were further investigated by Raman spectroscopy and compared with pure GNs. As illustrated in Fig. S3a (ESI†), the peaks located at 1340 cm^{-1} and 1582 cm^{-1} are clearly tracked for all three samples, which can be ascribed to the D band and the G band, respectively.[5] The I_D/I_G values calculated for Sn@C, Sn@C–GNs and GNs were 0.97, 0.98, and 1.13, respectively. The intensity ratios I_D/I_G for Sn@C and Sn@C–GNs are similar, indicating that the layered carbon shells in Sn@C–GN composites mainly contribute to the Raman signal and the partially disordered crystal structure as demonstrated in HRTEM images. The composites also exhibit a lower value of I_D/I_G compared with that of pure GNs, indicating the bigger size of the in-plane sp^2 domains and improved graphitic crystallinity. As a result, good conductivity could be expected for the core–shell hybrids. Thermal gravimetric analysis (TGA) was also carried out in air to quantify the carbon and tin content in the Sn@C and Sn@C–GN composites, as shown in Fig. S3b (ESI†). Carbon was oxidized to CO_2 from 200 °C to 650 °C with a corresponding weight loss of 11.35% for Sn@C composites and 22.04% for Sn@C–GNs. TGA data of pure Sn are also given for comparison and clarification, where Sn shows a trace of increase in weight due to slight oxidation. Therefore, neglecting the oxidation effect of tin (only around 1% in the temperature zone), the tin contents in Sn@C and Sn@C–GNs are calculated to be 88.65% (100–11.35%) and 77.96% (100–22.04%), respectively.

The study of the electronic structure of each component in the composite and the interaction between the Sn core and the carbon shell or GNs is crucial for understanding and optimizing the synergic effect in hierarchical Sn@C–GN composites employed as anodes for LIB. XANES is a spectroscopic technique which probes the local structure and bonding of an element of interest. By probing the unoccupied electronic states of the absorbing atom with a tunable synchrotron light source across an absorption edge, one can probe the local chemical environment and occupation (densities of states) of defect states as well as the conduction band. The interaction between Sn and carbonaceous materials could be unveiled by performing the XANES scans at the Sn L_3 (2p–5s, 5d) and C K (1s–2p) edges, studying the change of electronic structure and the local chemistry environment.

Fig. 3a shows the total electron yield (TEY) spectrum of Sn@C–GNs at the Sn L_3 edge. The spectra of SnO_2 and Sn nanoparticles are also shown for comparison. It can be seen that the surface sensitive TEY spectra of Sn@C–GNs are similar to those of Sn nanoparticles while obviously different from those of SnO_2 nanoparticles. For SnO_2 nanoparticles, they exhibit

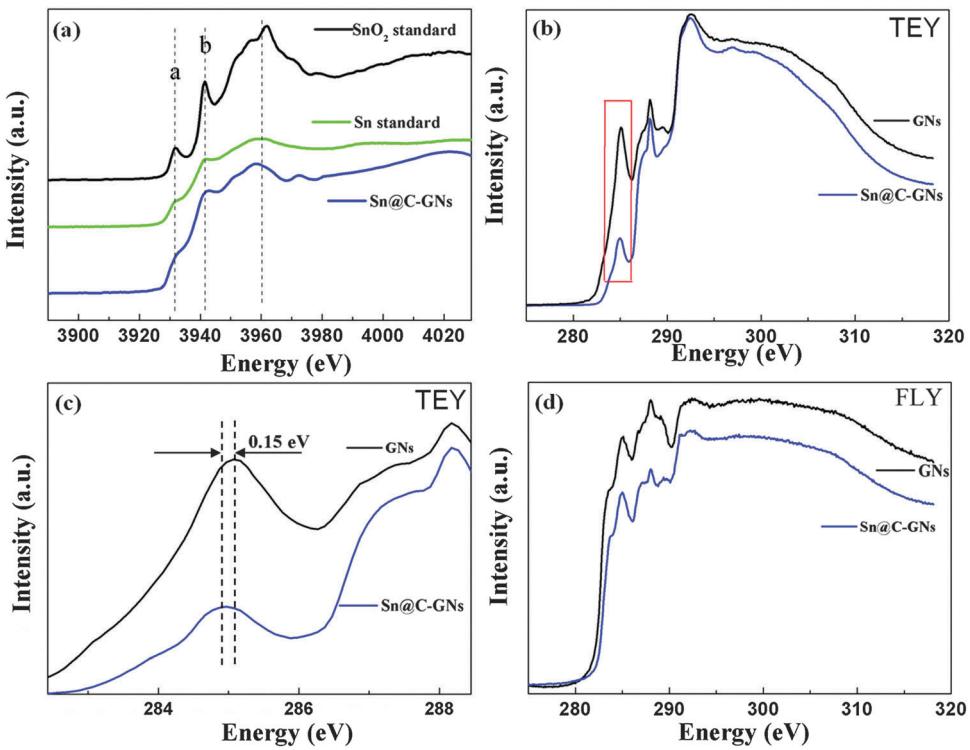

Fig. 3 (a) TEY spectrum at the Sn L_3 edge for Sn@C–GNs, Sn and SnO_2 nanoparticles. Carbon K-edge XANES for Sn@C–GNs and GNs: (b) TEY spectrum, (c) magnified TEY spectrum and (d) FLY spectrum.

obvious electron transitions from Sn 2p orbitals into unoccupied states with hybrid s and d character; the sharp peaks indicate localized electronic states, while for Sn and Sn@C–GNs, the resonance is less intense and broader, indicating a transition to the free electron like conduction band above the Fermi level.[30,31] The excitation peak for Sn@C–GNs shows that the Sn nanoparticles in Sn@C–GN composites are metallic. Besides, the more quenched and broader two pre-edge peaks ''a'' and ''b'' compared with pure SnO_2 nanoparticles also indicate the free electron like valence characteristics of Sn in Sn@C–GN composites. Spectra presented here indicate that Sn nanoparticles are well protected from oxidation by the carbon shell in hierarchical composites, which is reasonable since Sn@C–GN composites are synthesized by a reductive CVD process.

To further investigate the interaction between Sn and carbonaceous materials, carbon K-edge XANES was also performed on Sn@C–GN composites and compared with pure graphene in both TEY and X-ray fluorescence yield (FLY) modes, as shown in Fig. 3b–d. For GNs, characteristic peaks of the graphitic structure can be easily tracked at 285.1 eV for π^* transitions and at 291.5 and 292.5 eV for σ^* transitions.[32] The broad peak at 288.3 eV indicates the existence of a carboxylic group. In contrast, the Sn@C–GNs exhibit a similar resonance for σ^* transitions and the carboxylic group and a relatively low resonance for π^* transitions in the TEY spectrum. It should be noted that in Sn@C–GNs, two kinds of carbons from GNs and a partially crystallized carbon shell both contribute to the electron transition from carbon 1s to previously unoccupied electronic states. The π^* states have the same symmetry and are related to perpendicular orientation of the molecular orbital (axis) of the π^* orbital in benzene or graphite. Combining the HRTEM image of the carbon shell, which also shows the layered graphene-like structure, its XANES is expected to be similar to that of GNs except for a lower absorption intensity at the 1s to C–C π^* orbital transition. This is reasonable since the shell is near spherical and will exhibit little polarization dependence. Considering that the partially crystallized carbon is composed of staggered and shortened carbon basal planes, the irregular orientation at the perpendicular direction of the π^* orbital could cause low probability of π^* excitation. Fig. 3c shows the magnified spectrum of the red square region in Fig. 3b, it is clearly observed that for Sn@C–GN composites, the TEY spectrum exhibits a slight energy shift of 0.15 eV to lower excitation energy compared with that of pure GNs, illustrating that carbon atoms accept the electrons donated by Sn nanoparticles. The shift of energy is consistent with the notion that Sn–C shell interaction *via* charge redistribution indeed takes place between Sn nanoparticles and carbonaceous materials, favoring the immobilization of Sn onto surrounding carbon atoms. Such charge transfer from Sn to C 2p-derived π^* states in graphene or carbon shell could also result in a reduced π^* transition intensity (proportional to unoccupied density of states, pending no countervailing symmetry arguments). Turning to the FLY spectrum (Fig. 3d), which is bulk sensitive and the features are broadened due to the saturation effects (the fluorescence photon is reabsorbed by the sample); despite the broadening, the decreased intensity for Sn@C–GNs compared with pure GNs at π^* states was also observed. It should be noted that the peak intensity at 288.3 eV also decreases, this may indicate the decrease in carboxylic groups after the reductive CVD with ethylene. From these results, charge transfer and chemical bonding between Sn and carbonaceous materials in Sn@C–GN composites are clearly evident.

Fig. 4a shows the Sn K edge spectrum for Sn@C–GNs, Sn foil and SnO_2 nanoparticles. It can be seen that all three samples show a high-energy K edge centered at around 29.2 keV. SnO_2 nanoparticles exhibit a broad edge jump at around 29 210 eV while Sn@C–GN composites and Sn show a similar edge jump centered at 29 206 eV. The high energy resonance for SnO_2 should be attributed to the higher Sn(IV) ions. For Sn@C–GNs, Fig. 4b shows Fourier transform magnitudes of the Sn K edge extended X-ray absorption fine structure (EXAFS) spectrum for Sn@C–GNs, in comparison with those of reference Sn foil and SnO_2 materials. Tin oxides show typical FT peaks of Sn–O bonding at 1.45 Å for Sn^{4+}–O and a Sn–O–Sn bonding above 3 Å, while the Sn metal gives a FT peak of Sn–Sn metallic bonding at about 2.9 Å. For Sn@C–GNs, there are FT peaks of Sn–Sn metallic bonding at about 2.57 Å and Sn–C bonding in the surface region at 1.7 Å.[32] The peak feature without the peak [Sn–O–Sn] means that Sn are well protected by the carbon shell from oxidation. As a result, the as-prepared Sn metallic state can be supported with the help of the carbon shell. More intriguingly, the decreased Sn–Sn bonding length (2.57 Å) in the Sn@C–GN composites compared with that of standard tin foil (2.9 Å) indicates that the Sn lattice is compressed by the surrounding carbon atoms, in combination with the electron transfer and appearance of the Sn–C bond, the spectrum features indicate the intimate contact (chemical bonding and lattice compression) at the molecular scale between the Sn core and surrounding carbon atoms. A schematic diagram reflecting the bond variations and charge redistribution is illustrated in Fig. 4c.

The cyclic voltammetry plots of the Sn@C–GN composites are shown in Fig. 5a. In the first cathodic scan, the peaks positioned at 0.65 V and 0.35 V are referenced to the alloying process of lithium into tin forming Li_xSn,[18] while the peak at 0 V is referenced to the intercalation of lithium into the carbon shell and graphene forming LiC_6. Turning to the anodic process, the weak and broad oxidation peak at $\sim$0.12 V stands for the lithium extraction from the carbon or GNS. A series of peaks between 0.4 and 0.8 V are assigned to the de-alloying reaction of Li_xSn.[21] It can be seen that the plots of the second and third scans are almost overlapped, indicating that good electrochemical reversibility of lithium storage in the Sn@C–GN composites starts from the second cycle. In contrast, CV curves for Sn@C without GNs are shown in Fig. S3 (ESI†). The continuous decreased current intensity along with cycles demonstrates their poor stability. Fig. 5b presents the first two charge and discharge profiles of the composites at a current density of 75 mA g^{-1} with a voltage range of 0.01–3 V. The initial discharge curve exhibits a long slope starting from around 0.9 V to 0 V accompanying two small plateaus located at 0.65 V and 0.35 V, which can be assigned to the alloying of lithium with tin and intercalation of lithium into carbon or graphene reactions. This observation is in good agreement with the CV curves shown above.

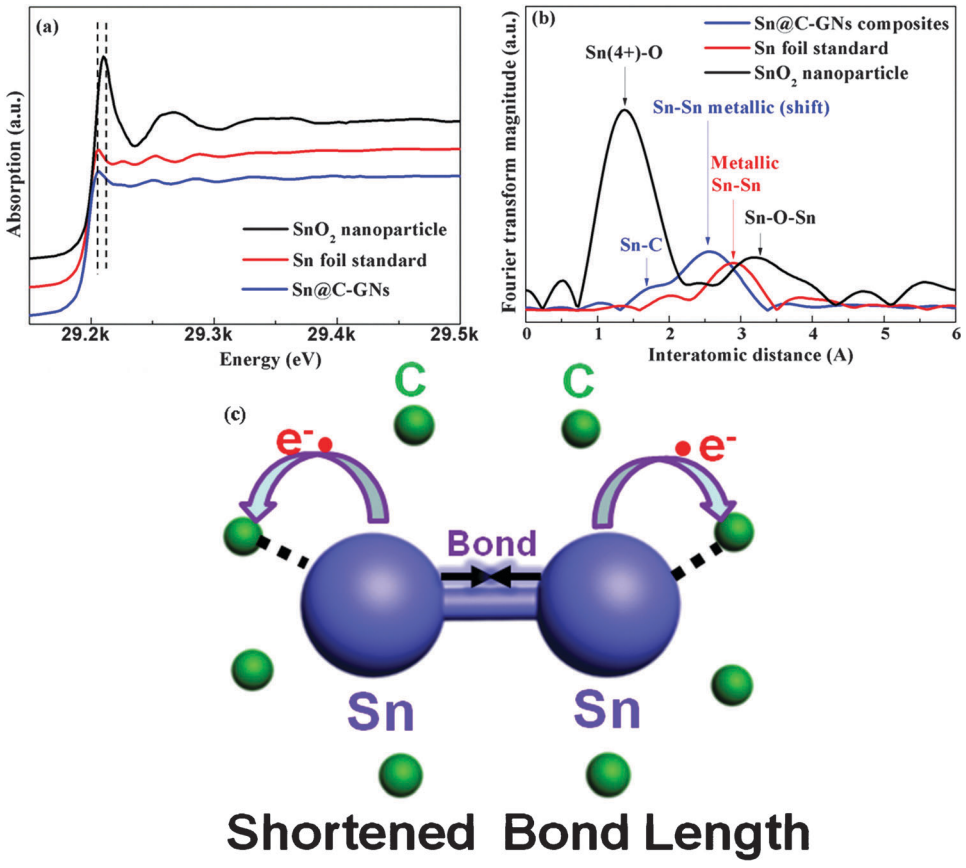

Fig. 4 (a) XANES spectrum at the Sn K edge and (b) Fourier-transformed (FT) magnitudes of Sn K edge k^3-weighted EXAFS spectra for Sn@C–GNs, SnO_2 nanoparticles and Sn foil. (c) The schematic representation of chemical bonding and lattice compression in Sn@C–GN composites.

Further, the nanocomposites clearly deliver a high initial discharge capacity of 1069 mA h g^{-1}. Most probably due to the solid electrolyte interphase formation on low crystallized carbon, the capacity fades to 750 mA h g^{-1} in the second discharge cycle.[21–23]

To evaluate the lifetime of Sn@C–GN composite electrodes during cycling, galvanostatic long term cycles measurement was carried out, as shown in Fig. 5c. For comparison, Sn@C composites without GNs and pure GNs were also performed at the same current density of 75 mA g^{-1} with a voltage range of 0.01–3 V. As we reported previously,[33,34] GNs achieve a high discharge capacity of 788 mA h g^{-1} initially followed by an obvious fading in the following cycles, maintaining only 270 mA h g^{-1} in the 100th cycle. For the Sn@C composites without GNs, however, the discharge capacity also decreases despite the high specific capacity of 1036 mA h g^{-1} at the initial cycle, and only delivers a lithium storage capability of 188 mA h g^{-1} at the 100th cycle. The poor cycle performance of Sn@C composites without GNs indicates that the outer carbon shell could not effectively buffer the volume change of the wider size distribution of the inner Sn core and prevent resultant pulverization of electrodes. In contrast, after hybridizing with GNs, the Sn@C–GNs exhibits both excellent cycle stability and high specific capacity. The initial discharge capacity could reach as high as 1069 mA h g^{-1}. More importantly, after 100 cycles, the discharge capacity still remains at 566 mA h g^{-1} which is more than two and three times of those for bare GNs and Sn@C without GN composites. We propose that the prolonged lifetime is due to (1) better confinement of the thick carbon shell in the composite with GNs compared with that in Sn@C composites without GNs; (2) improved mechanical properties provided by the flexible and robust GN supports and the outer carbon shell; (3) the well spatially separated Sn@C nanoparticles with uniform size; (4) the minimized aggregation of GNs due to deposition of Sn@C nanoparticles; (5) the extra voids between the Sn core and the carbon shell. Considering the state-of-the-art of anodes such as commercial graphite, which is 372 mA h g^{-1}, the hierarchical composite demonstrates its superiority as a potential alternative anode. The Sn@C–GN nanocomposites also exhibit excellent rate capability compared with Sn@C composites, as illustrated in Fig. 5d. It can be seen that the composite still delivers a discharge capacity of 286 mA h g^{-1} when the current density was increased stepwise up to 3750 mA g^{-1}. More intriguingly, it is worth noting that once the current rate is reversed back to 75 mA g^{-1}, a stable discharge capacity of 560 mA h g^{-1} returns, which is comparable to that of the same cell cycled galvanostatically (566 mA h g^{-1} at the 100th cycle). This observation indicates that the Sn@C–GN nanocomposites can endure varying discharge rates while keeping high energy densities in the meantime, which is more than welcome especially for practical

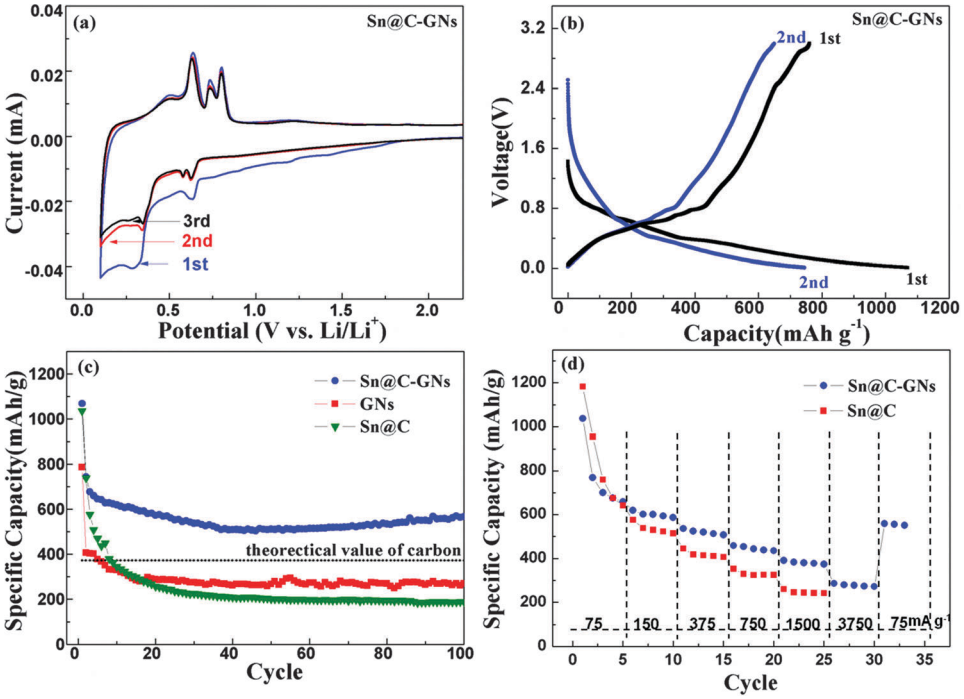

Fig. 5 (a) Cyclic voltammogram (CV) and (b) first two charge–discharge profiles of Sn@C–GN composites. (c) Cycle performance plots of bare graphene, Sn@C composites and Sn@C–GN nanocomposites at 75 mA g^{-1}. (d) Rate performance of Sn@C–GN and Sn@C composites.

applications in EVs. To our knowledge, the obtained electrochemical performance of hierarchical nanostructured Sn@C–GN composites is comparable or even superior to the literature reported Sn based and other core–shell Sn@C nanocomposites.[9,20,26,35–37] Combining the excellent electrical conductivity of GNs and the carbon shell, the hierarchical morphology of Sn@C–GNs, which facilitates electrolyte immersion, and the intimate contact between Sn nanoparticles and carbonaceous materials, fast electrons and lithium ion exchange rate can be realized.

To investigate the improved electrochemical performance of the hierarchical nanostructure, TEM was performed to examine the morphology variation of Sn@C with and without GN nanocomposite electrodes after 100 cycles. For Sn@C without GN electrodes, many exposed big Sn particles can be found and the carbon shell fractures and falls apart from the Sn core, indicating that the carbon shell could not maintain the volume change of Sn, which leads to the poor cycling. In contrast, for Sn@C–GNs, it reveals that the Sn nanoparticles were still embedded in the carbon shell and GN matrices without any obvious volume change (Fig. S4, ESI†), demonstrating that core–shell Sn@C is well kept and pinned onto the GNs during cycling. The result that Sn nanoparticles in the hierarchical composite showed less agglomeration and size variation should be ascribed to the good protection of the outer carbon shell and GNs, which effectively accommodate the strain and stress arising from the volume change of tin and avoid the detachment of active materials from the current collector during cycling. As a result, enhanced cyclic stability and rate capability were achieved. Thus, the Sn@C–GN nanocomposites can be applied as potential anodes in high performance LIBs.

Conclusions

Sn@C–GN composites have been successfully synthesized by an effective one-step CVD strategy. The core–shell nanostructured Sn@C composites embedded in GNs exhibit high lithium storage capacities compared with pure GNs and Sn@C composites without GNs due to the flexible carbon shell, the encapsulated voids between the Sn core and the carbon shell caused by Sn shrinkage, and GNs, which can buffer the huge Sn core volume change during cycling. The Sn@C–GNs also demonstrate excellent rate performance combining the hierarchical structure of Sn@C–GNs and the high electrical conductivity provided by the GNs and the carbon shell. XANES and EXAFS studies at the Sn K, M, L_3 edges and the C K-edge clearly demonstrate that chemical bonding, charge transfer and lattice variation take place between Sn and carbonaceous materials, which anchors the Sn nanoparticles into the carbon shell and GNs firmly and facilitates a fast charge transfer rate between Sn and carbonaceous materials. All these observations demonstrate that the hierarchical Sn@C–GNs can act as an alternative anode for EVs and HEVs applications and synchrotron spectroscopy glean a more complete understanding of the mechanism behind the improved performances.

Acknowledgements

This research was supported by Natural Sciences and Engineering Research Council of Canada (NSERC), General Motors of Canada, Canada Research Chair (CRC), Canada Foundation for Innovation (CFI), Ontario Innovation Trust (OIT) Program, X-ray Science Division (XSD)/Pacific Northwest Consortium (PNC) at Sector 20

of Advanced Photon Source and University of Western Ontario. The Canadian Light Source is supported by CFI, NSERC, NRC, CHIR, and the University of Saskatchewan.

References

1 A. S. Aricó, P. Bruce, B. Scrosati, J. M. Tarascon and W. V. Schalkwijk, *Nat. Mater.*, 2005, **4**, 366–377.
2 R. Bashyam and P. Zelenay, *Nature*, 2006, **443**, 63–66.
3 S. M. Paek, E. J. Yoo and I. Honma, *Nano Lett.*, 2009, **9**, 72–75.
4 X. W. Lou, C. M. Li and L. A. Archer, *Adv. Mater.*, 2009, **21**, 2536–2539.
5 J. Yang, J. Wang, D. Wang, X. Li, D. Geng, G. Liang, M. Gauthier, R. Li and X. Sun, *J. Power Sources*, 2012, **208**, 340–344.
6 Y. Idota, T. Kubota, A. Matsufuji, Y. Maekawa and T. Miyasaka, *Science*, 1997, **276**, 1395–1397.
7 D. Larcher, S. Beattie, M. Morcrette, K. Edstroem, J. C. Jumas and J. M. Tarascon, *J. Mater. Chem.*, 2007, **17**, 3759–3772.
8 I. A. Courtney and J. R. Dahn, *J. Electrochem. Soc.*, 1997, **144**, 2943–2948.
9 D. Deng and J. Y. Lee, *Angew. Chem., Int. Ed.*, 2009, **48**, 1660–1663.
10 J. Hassoun, G. Derrien, S. Panero and B. Scrosati, *Adv. Mater.*, 2008, **20**, 3169–3175.
11 G. Derrien, J. Hassoun, S. Panero and B. Scrosati, *Adv. Mater.*, 2007, **19**, 2336–2340.
12 K. T. Lee, Y. S. Jung and S. M. Oh, *J. Am. Chem. Soc.*, 2003, **125**, 5652–5653.
13 G. X. Wang, X. P. Shen, J. Yao and J. Park, *Carbon*, 2009, **47**, 2049–2053.
14 K. S. Novoselov, A. K. Geim, S. V. Morozov, D. Jiang, Y. Zhang, S. V. Dubonons, I. V. Grigorieva and A. A. Firsov, *Science*, 2004, **306**, 666–669.
15 K. S. Novoselov, A. K. Geim, S. V. Morozov, D. Jiang, M. I. Katsnelson, I. V. Grigorieva, S. V. Dubonons and A. A. Firsov, *Nature*, 2005, **438**, 197–200.
16 C. Berger, Z. M. Song, X. B. Li, X. S. Wu, N. Brown, C. Naud, D. Mayou, T. B. Li, J. Hass, A. N. Marchenkov, E. H. Conrad, P. N. First and W. A. de Heer, *Science*, 2006, **312**, 1191–1196.
17 S. Stankovich, D. A. Dikin, G. H. B. Dommett, K. M. Kohlhaas, E. J. Zimney, E. A. Stach, R. D. Piner, S. T. Nguyen and R. S. Ruoff, *Nature*, 2006, **442**, 282–286.
18 Z. S. Wu, W. C. Ren, L. Wen, L. B. Gao, J. P. Zhao, Z. P. Chen, G. M. Zhou, F. Li and H. M. Cheng, *ACS Nano*, 2010, **4**, 3187–3194.
19 G. M. Zhou, D. W. Wang, F. Li, L. L. Zhang, N. Li, Z. S. Wu, L. Wen, G. Q. Lu and H. M. Cheng, *Chem. Mater.*, 2010, **22**, 5306–5313.
20 G. Wang, B. Wang, X. Wang, J. Park, S. Dou, H. Ahn and K. Kim, *J. Mater. Chem.*, 2009, **19**, 8378–8384.
21 X. F. Li, X. B. Meng, J. Liu, D. S. Geng, Y. Zhang, M. N. Banis, Y. L. Li, J. L. Yang, R. Y. Li, X. L. Sun, M. Cai and M. W. Verbrugge, *Adv. Funct. Mater.*, 2012, **22**, 1647–1654.
22 J. Yao, X. P. Shen, B. Wang, H. K. Liu and G. X. Wang, *Electrochem. Commun.*, 2009, **11**, 1849–1852.
23 S. Ding, D. Luan, F. Boey, J. Chen and X. W. Lou, *Chem. Commun.*, 2011, **47**, 7155–7157.
24 J. S. Chen, Y. L. Cheah, Y. T. Chen, N. Jayaprakash, S. Madhavi, Y. H. Yang and X. W. Lou, *J. Phys. Chem. C*, 2009, **113**, 20504–20508.
25 X. W. Lou, J. S. Chen, P. Chen and L. A. Archer, *Chem. Mater.*, 2009, **21**, 2868–2874.
26 S. Q. Chen, P. Chen, M. H. Wu, D. Y. Pan and Y. Wang, *Electrochem. Commun.*, 2010, **12**, 1302–1306.
27 Y. Q. Zou and Y. Wang, *ACS Nano*, 2011, **5**, 8108–8114.
28 J. G. Zhou, H. T. Fang, J. M. Maley, J. Y. P. Ko, M. Murphy, Y. Chu, R. Sammynaiken and T. K. Sham, *J. Phys. Chem. C*, 2009, **113**, 6114–6117.
29 J. G. Zhou, H. T. Fang, Y. F. Hu, T. K. Sham, C. X. Wu, M. Liu and F. Li, *J. Phys. Chem. C*, 2009, **113**, 10747–10750.
30 T. K. Sham, *Phys. Rev. B: Condens. Matter Mater. Phys.*, 1985, **31**, 1888–1902.
31 T. K. Sham, *Int. J. Nanotechnol.*, 2008, **5**, 1194–1246.
32 M. Noh, Y. Kim, M. G. Kim, H. Lee, H. Kim, Y. Kwon, Y. Lee and J. Cho, *Chem. Mater.*, 2005, **17**, 3320–3324.
33 X. F. Li, D. S. Geng, Y. Zhang, X. B. Meng, R. Y. Li and X. L. Sun, *Electrochem. Commun.*, 2011, **13**, 822–825.
34 D. Wang, X. Li, J. Wang, J. Yang, D. Geng, R. Li, M. Cai, T. K. Sham and X. Sun, *J. Phys. Chem. C*, 2012, **116**, 22149–22156.
35 K. Hsu, C. Liu, P. Chen, C. Lee and H. Chiu, *J. Mater. Chem.*, 2012, **22**, 21533–21539.
36 B. Luo, B. Wang, M. Liang, J. Ning, X. Li and L. Zhi, *Adv. Mater.*, 2012, **24**, 1405–1409.
37 H. Liu, R. Hu, M. Zeng, J. Liu and M. Zhu, *J. Mater. Chem.*, 2012, **22**, 8022–8028.

